Back-propagating rupture evolution within a curved slab during the 2019 Peru intraslab earthquake

Yaping Hu*[, a], Yuji Yagi[b], Ryo Okuwaki[b, c, d], Kousuke Shimizu[a]

[a] Graduate School of Life and Environmental Sciences, University of Tsukuba, Ibaraki 305-8572, Japan
[b] Faculty of Life and Environmental Sciences, University of Tsukuba, Ibaraki 305-8572, Japan
[c] Mountain Science Center, University of Tsukuba, Ibaraki 305-8572, Japan
[d] COMET, School of Earth and Environment, University of Leeds, Leeds LS2 9JT, UK

Summary

The 26 May 2019 M_W 8.0 Peru intraslab earthquake ruptured the subducting Nazca plate at a point where the dip angle of the slab increases sharply and the strike angle rotates clockwise from the epicenter to north. To obtain a detailed seismic source model of the 2019 Peru earthquake, including not only the rupture evolution but also the spatiotemporal distribution of focal mechanisms, we performed comprehensive seismic waveform analyses using both a newly developed flexible finite-fault teleseismic waveform inversion method and a back-projection method. The source model revealed a complex rupture process involving a back-propagating rupture. The initial rupture propagated downdip from the hypocenter, then unilaterally northward along the strike of the slab. Following a large slip occurring 50–100 km north of the hypocenter, the rupture propagated bilaterally both further northward and back southward. The spatial distribution of focal mechanisms shows that the direction of T-axis azimuth gradually rotated clockwise from the epicenter northward, corresponding to the clockwise rotation of the strike of the subducting Nazca plate, and the large-slip area corresponds to the high-curvature area of the slab iso-depth lines. Our results show that the complex rupture process, including the focal-mechanism transition, of the Peru earthquake was related to the slab geometry of the subducting Nazca plate.

Keywords: earthquake rupture process, finite-fault inversion, back projection, T-axis azimuth rotation, slab geometry.

* Corresponding Author

yaping-hu@geol.tsukuba.ac.jp (Yaping Hu)

1. Introduction

On 26 May 2019, a great normal-fault earthquake struck Peru and adjacent areas. The U.S. Geological Survey (USGS) determined the origin time to be 07:41:15 (UTC) on 26 May 2019, the hypocenter to be 122.6 km deep at 5.812°S, 75.270°W, and the moment magnitude to be (M_W) 8.0. The 2019 Peru earthquake is the largest event ever recorded in northern Peru (Wong et al., 2012; Villegas-Lanza et al., 2016), one of the most seismically active zones in the world (Perfettini et al, 2010; Sladen et al., 2010), where the oceanic Nazca plate is subducting beneath the South America plate (Somoza and Ghidella, 2005; Prezzi and Silbergleit, 2015) (Fig. 1). The distribution of hypocentral depths of intermediate-depth (60–300 km) earthquakes near the source region is consistent with slab depth changes. According to the Global Centroid Moment Tensor (GCMT) catalog (Dziewonski et al., 1981; Ekström et al., 2012), the focal mechanism of most intraslab earthquakes is normal faulting (Fig. 1). Before the 2019 Peru earthquake, high seismicity was observed in slab-bending zones, such as between 1.0°S and 2.5°S, and between 7.5°S and 9.5°S, but no large earthquake had been recorded in the source area of the 2019 event.

In general, knowledge of the distribution of focal mechanisms is needed to understand the stress field in a slab (Wang et al., 2004; Chang et al., 2019). The fault plane orientation of most intraslab events has been approximately parallel to the slab geometry (Slab2 model, Hayes et al., 2018), and the azimuthal directions of the T-axes of these normal-fault earthquakes are roughly perpendicular to the depth contours of the slab (Fig. 1). The general trend of the T-axis azimuths is the representative of the principal tensional stress axes in this region (Tavera and Buforn, 2001). Because great intraslab earthquakes rupture large areas, a heterogeneous spatial distribution of focal mechanisms is expected because of the heterogeneity of stress fields related to the slab geometry. To understand the relationship between slab geometry and the rupture process, including focal mechanism variation during large earthquakes, it is important to determine the spatio-temporal distribution of seismic potency density tensors of great intraslab earthquakes (i.e., spatiotemporal distribution of slip and the fault geometry).

Recently, Shimizu et al. (2020) developed a flexible finite-fault inversion method that takes account of the uncertainty of the Green's function, following Yagi and Fukahata (2011), and represents fault slip by the superposition of five basis double-couple components (Kikuchi and Kanamori, 1991). The developed flexible finite-fault inversion method not only reduces the effect of modeling errors originating from the uncertainty of the assumed fault geometry but also allows us to estimate the spatio-temporal distribution of focal mechanisms and potency density (hereafter called slip) on the modeled fault plane. In this study, we applied the flexible finite-fault inversion method to the teleseismic body waves of the 2019 Peru earthquake, and then estimated the T-axis azimuth distribution of the obtained focal mechanism distribution to evaluate the relationship between T-axis azimuth variation and the stress field related to the slab geometry. We set a realistic model plane and then estimated fault slip occurring in the vicinity of the assumed model plane. Hereafter, we refer to this model plane as the fault plane.

One problem in interpreting the source model of an intermediate-depth earthquake is that it is generally difficult to select the primary fault plane from the two possible nodal planes obtained by moment tensor inversion (e.g., the GCMT solution). Because of the low aftershock activity of most intermediate-depth earthquakes, including the 2019 Peru earthquake, the aftershock distribution may not directly indicate the primary fault plane. In this study, the primary fault plane of the 2019

Peru earthquake was evaluated by the integrated use of waveform inversion and back-projection (BP). BP is useful for tracking the spatiotemporal source evolution of specific seismic phases during large earthquakes (Ishii et al., 2005; Krüger and Ohrnberger, 2005), but the depth resolution of the method is generally low (Yagi et al., 2012; Kiser and Ishii, 2017). In contrast, finite-fault inversion results for teleseismic body waves have good resolution in the depth direction (e.g., Yagi et al., 2004). Complementary use of BP and finite-fault inversion thus helps us to estimate both the rupture evolution and the primary fault plane. Finally, we compared the distributions of high-frequency radiation sources and potency-rate density (called slip rate hereafter) on the primary fault plane and then constructed an integrated source model from which we inferred the detailed rupture process of the 2019 Peru earthquake.

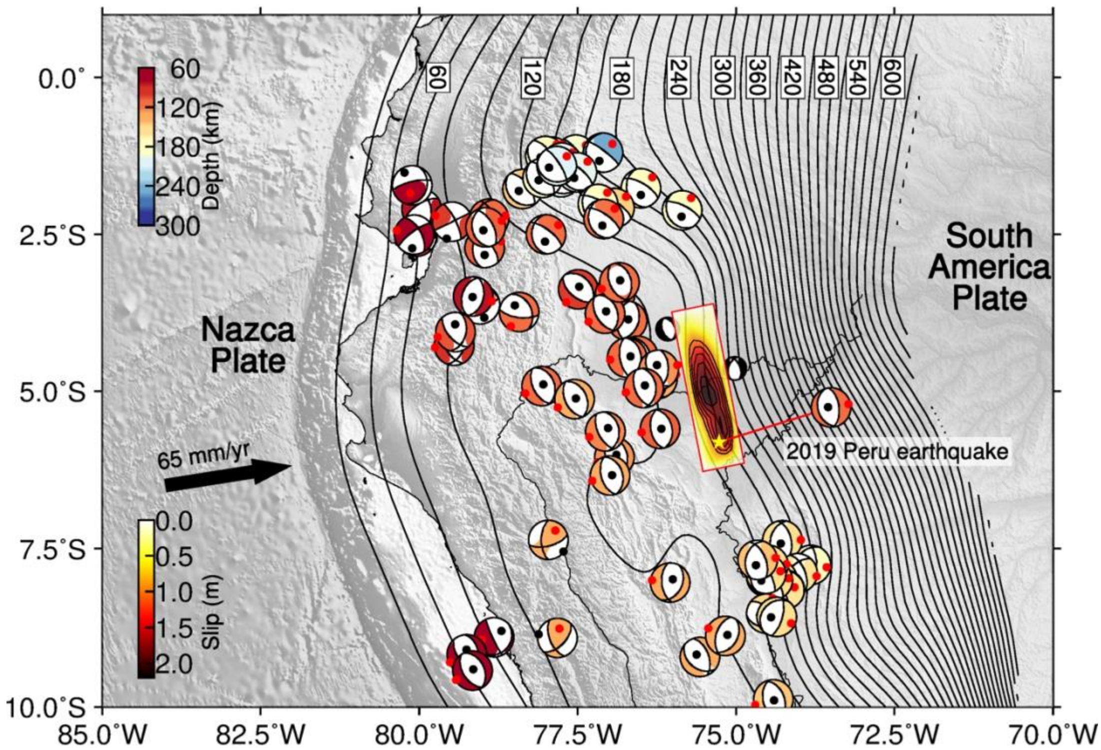

Figure 1: Overview of the source region of the 2019 Peru earthquake. Black lines indicate depth contours of Slab2 model (Hayes et al., 2018) at an interval of 20 km. The beach balls show the GCMT solutions of the Mw > 5.5 intermediate-depth earthquakes (depth: 60–300 km) that occurred in 1976–2019. Black and red dots in beach balls denote P-axis and T-axis, respectively. The color of beach balls represents depth. The black beach balls are the aftershocks of the Peru earthquake within one month. Black arrow shows the relative motion of the Nazca plate (DeMets et al., 2010). The red rectangle and yellow stars show the primary fault plane and the epicenter of the main shock, respectively. The color contour shows slip, with an interval of 0.4-m slip.

2. Data and methods

We used the vertical components of teleseismic *P*-wave data from the Data Management Center of the Incorporated Research Institutions for Seismology (IRIS-DMC) recorded by stations within an epicentral distance between 30° and 90°. Teleseismic *P* waveforms recorded at 41 stations with adequate quality and good azimuthal coverage were selected for use in both the finite-fault inversion and BP (Fig. 2). We chose the teleseismic *P* waveform because of its well-defined data covariance components in the inversion formulation (Yagi and Fukahata, 2011) and its clear first-motion rise, which can be reliably picked. The first motion of the *P*-phase was manually picked, and the data were converted to velocity data. Then, the velocity waveforms were resampled at 0.8 s intervals for the finite-fault inversion.

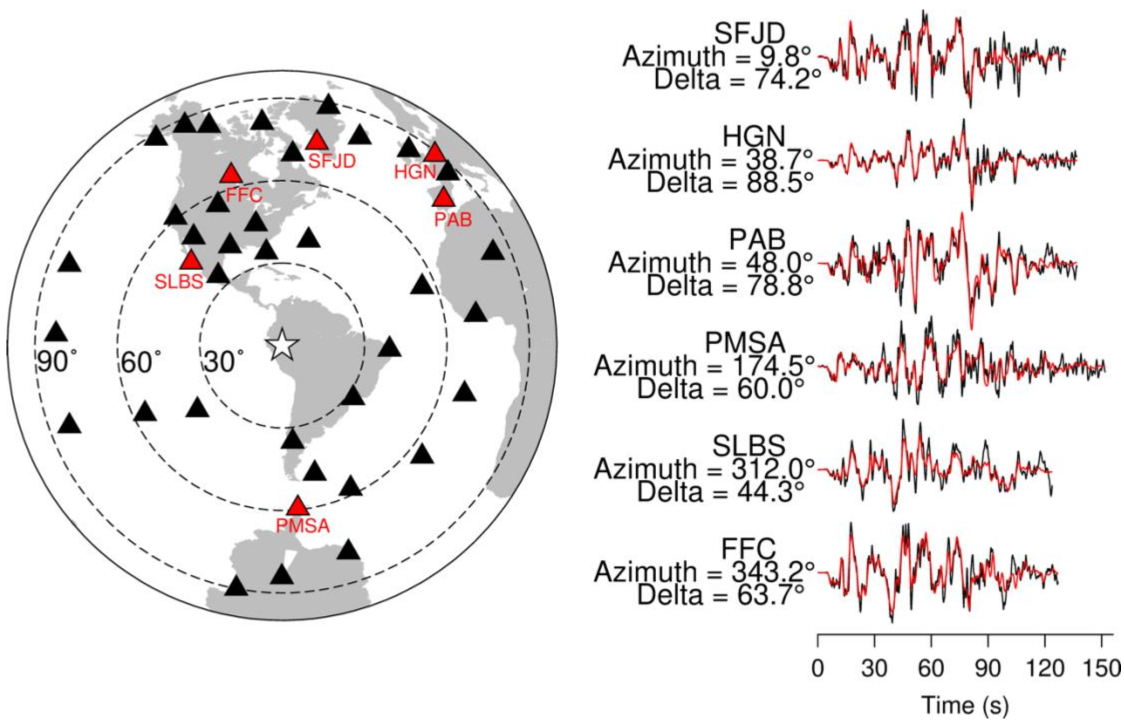

Figure 2: Distribution of teleseismic stations (triangles) and selected waveform fitting between observed (black lines) and synthetic waveforms (red lines). Red star denotes the epicenter of the Peru earthquake determined by USGS. Station code, azimuth and epicentral distance are shown on the right of each waveform fitting.

Finite-fault inversion has been widely used since the 1980s for estimating the spatiotemporal slip-rate distribution of earthquakes (e.g., Olson and Apsel, 1982; Hartzell and Heaton, 1983). A linear finite-fault inversion can be used to obtain the slip-rate distribution on an assumed model plane. However, because we never know the true velocity structure under the surface and can hardly get the detailed information of fault geometry, the uncertainty of the Green's function and the uncertainty of the fault geometry together make it difficult to estimate seismic source models in a stable manner (e.g., Yagi and Fukahata, 2011; Duputel et al., 2014; Ragon et al., 2018; Shimizu et al., 2020). Recently, Shimizu et al. (2020) proposed a flexible finite-fault inversion method that mitigates the effect due to the uncertainty of the fault geometry by obtaining the distribution of seismic potency tensors along the assumed model plane, and that also mitigates the effect of the uncertainty of the Green's function by appropriately setting the data covariance matrix following Yagi and Fukahata (2011). In the flexible finite-fault inversion method, fault slip along the assumed model plane is represented by the superposition of five basis double-couple components (Kikuchi and Kanamori, 1991); then, the possible fault geometry can be inferred from the spatiotemporal variation of focal mechanisms. Thus, to reveal both the slip-rate evolution and fault geometry of the 2019 Peru earthquake, we applied flexible finite-fault inversion to teleseismic *P* waves.

In this study, we set a model plane and assumed that fault slip occurred in the vicinity of this model plane (called the "fault plane" hereafter). Because it is difficult to select the primary fault plane from the two nodal planes of a moment tensor solution, we tested two different fault plane geometries (called N1 and N2) based on the USGS W-phase moment tensor solution (N1: strike = 350°, dip = 53°; N2: strike = 166°, dip = 37°) (https://earthquake.usgs.gov-/earthquakes/eventpage/us60003sc0/moment-tensor). For both the N1 and N2 models, we considered the fault plane to be 270 km long and 105 km wide, with a total of 18 grid cells along the strike and 7 grid cells along the dip spaced at 15 km intervals in both the strike and dip directions. The theoretical Green's function with a sampling rate of 0.1 s was calculated by the method of Kikuchi and Kanamori (1991). We adopted the hypocenter determined by the USGS as the initial rupture point. For the velocity structure model near the source, we used a one-dimensional velocity model modified from the inferred velocity structure in the Peru region (Kaila et al., 1999; Ma and Clayton, 2014) (Table 1). The travel time, ray parameters, and geometrical spreading factors were calculated based on the ak135 reference velocity model (Kennett et al., 1995). As the slip-rate function at each source node, we adopted a linear B-spline function with a temporal interval of 0.8 s and a maximum duration of 55 s, and we assumed the slip rate to be zero after 80 s. We tested maximum rupture-front velocities from 2.5 to 5.0 km/s (Fig. S1). In the range of 2.5 to 3.5 km/s, the major rupture area expanded as the assumed maximum rupture-front velocity increased, but in the range of 4.0 to 5.0 km/s (Fig. S1a), this dependency became indistinct. In addition, fluctuations of the moment rate function (Fig. S1b) were similar among the tested rupture-front velocities. The first peak was during 0–15 s (the initial rupture), and the largest peak was during 15–80 s (the main rupture). On the basis of these results, we selected 4.5 km/s as the optimum rupture-front velocity.

Table 1. Velocity model used for calculating Green's function

V_P (km/s)	V_S (km/s)	Density (10^3 kg/m^3)	Thickness (km)
6.00	3.47	2.70	20
6.66	3.85	2.90	20
7.10	4.13	3.05	30
7.80	4.50	3.25	30
8.10	4.70	3.38	90
8.60	5.00	3.55	0

BP is a method used to obtain the spatio-temporal distribution of seismic radiation sources by waveform stacking that can provide information on rupture acceleration and deceleration (e.g., Uchide et al., 2013; Okuwaki et al., 2014). The 2019 Peru earthquake was an intermediate-depth earthquake. Because the *P* phase and the later depth phases were well separated, possible contamination by the depth phases was avoided, making it possible to acquire less-biased BP images (e.g., Suzuki and Yagi, 2011) from which to reliably estimate rupture velocity and, therefore, infer the detailed rupture evolution. In our study, we used the BP method to obtain the primary fault plane and to infer the detailed rupture process, including rupture acceleration and deceleration. To enable comparison of the BP results with those of the finite-fault inversion, we used the same velocity waveform dataset and the same model settings for BP as for waveform inversion (Figs. 2 and S2). A Butterworth band-pass filter from 0.2 to 2.0 Hz was applied to the velocity waveforms, and then the data were resampled at 0.05 s intervals. We adopted nonlinear *n*th root stacking (n = 3) (Muirhead and Datt, 1976) to improve the signal-to-noise ratio of the BP images. The same fault plane as was adopted for the inversion analysis was used as the possible source area for the BP imaging, but the spatial grid interval of the possible source area was set to 1 km so that high-frequency radiation sources could be resolved.

3. Results

We constructed two seismic source models, one for each of the two fault plane geometries, N1 and N2 (Fig. 3). In both the N1 and N2 models, the rupture is concentrated in the area from 30 km south to 200 km north of the hypocenter in the along-strike direction. Rupture propagation is downdip on both two fault planes; while, the rupture propagates eastward on the N1 fault plane and westward on the N2 fault plane. The focal mechanisms in the large-slip area indicate normal faulting, but a small strike-slip component was obtained in the small-slip areas at the northern and southern edges of each fault plane (Figs. 3c, d). In both models, the T-axis azimuth, extracted from the resultant potency-density tensors, gradually rotate in the clockwise direction from the hypocenter toward the northern end of the major rupture area (Figs. 3e, f). T-axis azimuths in the small-slip area are outside of the 62° to 92° range of the azimuths in the large-slip area, possibly because of contamination by later phases and the relatively small slip amplitudes at the northern and southern edges of the fault plane. The inverted total seismic moment was 1.84×10^{21} Nm (M_W 8.1) for the N1 fault plane and 1.89×10^{21} Nm (M_W 8.1) for the N2 fault plane; these values are slightly larger than both the USGS solution of 1.14×10^{21} Nm (M_W 8.0) and the GCMT solution of 1.23×10^{21} Nm (M_W 8.0). The waveform fittings between observed and synthetic waveforms show good agreement, with a variance of 0.270 for the N1 model and 0.267 for the N2 model.

Figure 4 shows snapshots of the N1 and N2 models. In both models, the rupture propagates downdip from the hypocenter for 15 s after the initial break. In the N1 model, however, the initial rupture propagates eastward, whereas it propagates westward in the N2 model. From 15 to 30 s after the initial break, the rupture propagates unilaterally northward in both models. Then at 30 s, the rupture begins to propagate bilaterally toward both the north and south, and a large slip occurs on the downdip side of the hypocenter near where the initial rupture occurred in both models. Then, 45 s after the initial break, the rupture propagates unilaterally northward again. The rupture finally stops about 200 km north of the epicenter. A synthetic test performed to evaluate the robustness of the waveform inversion result showed that the output model could well restore the input model (see Text S1).

We also performed BP with fault planes N1 and N2 by computing the travel times between the possible sources and the stations. We identified five major radiation events, labeled A to E, having BP signals with relatively strong intensity (Figs. 4 and 5). In both models, event A appears east of the epicenter during the initial rupture process (within ~15 s of the initial break) (Fig. 4). From 15 to 30 s, event B is seen around 20 to 80 km north of the epicenter. Events C and D are observed from ~35 to 40 s and from ~40 to 50 s after the initial break, but while the former appears around 20 km south of the epicenter, the latter appears 100 km north of the epicenter. Event E appears 150 km north of the epicenter from ~50 to 55 s after the initial break.

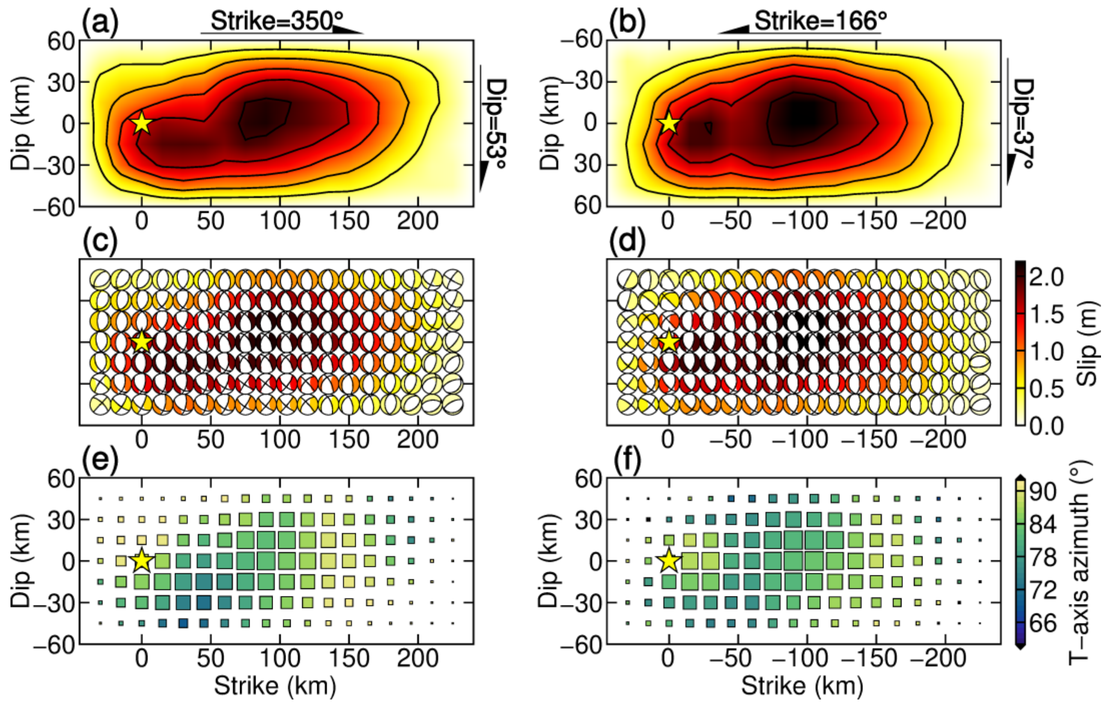

Figure 3: Finite-fault inversion results of two possible nodal planes (N1: strike=350°, dip=53°; N2: strike=166°, dip=37°). Top and middle figures represent the spatial distribution of the slip and focal mechanisms, respectively. The focal mechanism, plotted by using a lower-hemisphere stereographic projection, is not rotated according to the model plane setting. The contour is 0.4 m. The bottom figures show the distribution of T-axis azimuths. The size of the square scales with slip. The star is the hypocenter.

4. Discussion

4.1. Evaluation of the primary fault plane of the 2019 Peru earthquake

In ordinary finite-fault inversion, the selection of the primary fault plane from the two possible nodal planes obtained from the moment tensor solution is usually based on the aftershock distribution or the surface rupture geometry; then, the slip-rate distribution is estimated for the selected fault plane (e.g., Legrand and Delouis, 1999). However, for an intermediate-depth earthquake associated with low aftershock activity such as the 2019 Peru earthquake, it is difficult to uniquely identify the primary fault plane. It might be possible to select the primary fault plane if the main rupture propagation direction can be determined by examining the pulse width of the observed waveforms (e.g., Legrand and Delouis, 1999). However, even if a seismic source model in which both planes satisfy the major rupture direction can be constructed, selecting the primary fault plane is still difficult because for both fault planes the waveform variances between synthetic and observed waveforms would have nearly identical values (e.g., Julian et al., 1998; Ye et al., 2020). In fact, the variance of the waveform fittings differed by less than 1.2% between our N1 and N2 models. Therefore, determination of the primary fault plane of the 2019 Peru earthquake by only finite-fault inversion is not possible.

In general, the Green's function of teleseismic body waves describes not only the direct *P* phase but also phases reflected from the ground surface in the near-source region (i.e., the *pP* and *sP* phases), which contain useful information on the depth of the radiation source. In finite-fault inversion, a high resolution in the depth direction can be obtained that can explain waveforms overall, including the reflected phases (e.g., Yagi et al., 2004). In our study, snapshots of the slip distribution on the N1 and N2 fault planes show spatial differences in rupture propagation (Fig. 4). During the initial rupture, the finite-fault inversion for the N1 model resolved an eastward downdip rupture, whereas the N2 model showed downdip westward propagation. Thus, in both the N1 and N2 models, the finite-fault inversion had good resolution in the depth direction, as shown by the downdip propagation of the initial rupture in both models, but not in the horizontal rupture direction. In contrast, the BP results showed that the initial rupture propagated eastward on both fault planes (Fig. 4). Similarly, in the finite-fault inversion result for the main rupture on the southern part of the fault plane, the inverted slip near the hypocenter from 35 to 45 s is on the east and west side of the hypocenter in the N1 and N2 model, respectively. In contrast, the BP results showed that *P*-waves with strong intensity radiated eastward from the epicenter on both fault planes. Given the consistency of the rupture direction on the N1 fault plane between the inversion and BP imaging results, the rupture paths are located to the east of the epicenter. We additionally note that the BP signals for the main rupture from 40 to 45 s showed stronger high-frequency radiation in the N1 model (Fig. 4a). We therefore selected the eastward-dipping N1 fault plane as the preferred fault plane for the 2019 Peru earthquake.

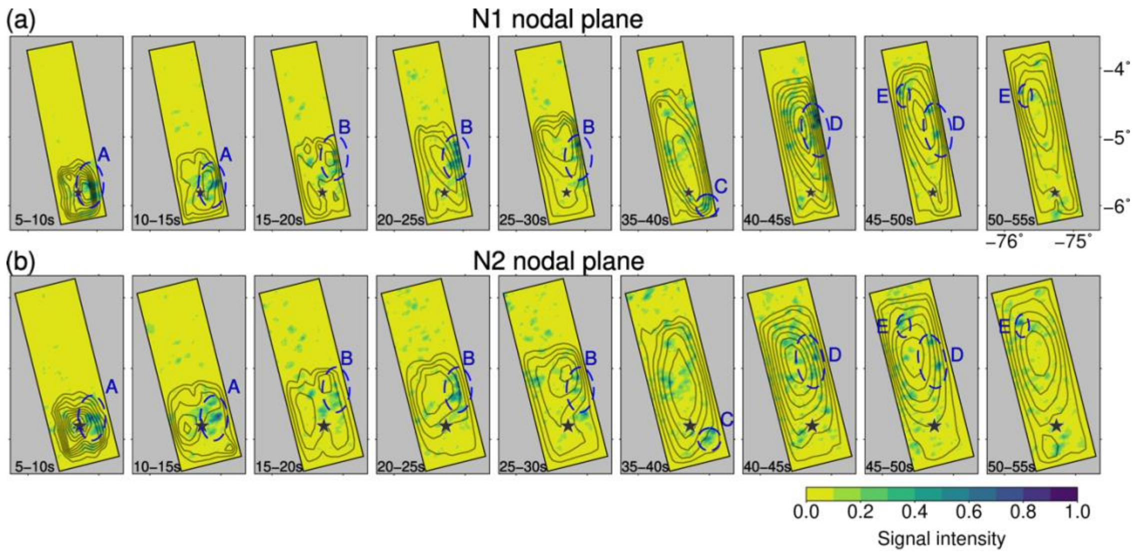

Figure 4: Snapshots of N1 and N2 models. The distribution of average slip-rate (contours) and normalized high-frequency radiation (color scale) are obtained by finite-fault inversion and BP analyses, respectively. The BP signals are marked as Event A to E (blue dashed circles). The time window of each snapshot is on left-bottom. The color represents the normalized strength of high-frequency radiation. The black star indicates the epicenter. The black contour interval of slip-rate is 0.02m/s.

4.2. Detailed rupture process with a back-propagating rupture

The initial rupture begins around the hypocenter at 0 to 5 s and then propagates downdip from the hypocenter at a high slip rate. From 15 s, the rupture propagates northward from the epicenter, and a high slip rate is observed north of the epicenter during 15 to 30 s (Fig. 5). The strong BP signals of event A appear to the east of the epicenter at 5 s, and then move north of the epicenter from 10 to 15 s. It is known that intense high-frequency waves can be radiated as a result of a rapid change of rupture-front velocity, slip velocity, or both (e.g., Madariaga, 1977; Spudich and Frazer, 1984; Yagi and Okuwaki, 2015). The multiple energy burst spots of event A located around the rupture front correspond to fluctuations in the rupture propagation rate. The first peak of the moment rate function (Fig. S1b) also suggests that the first rupture with small seismic energy occurs during 0 to 15 s. We therefore inferred that, following the initial rupture propagation downdip from the hypocenter, the rupture propagated unilaterally northward from the epicenter.

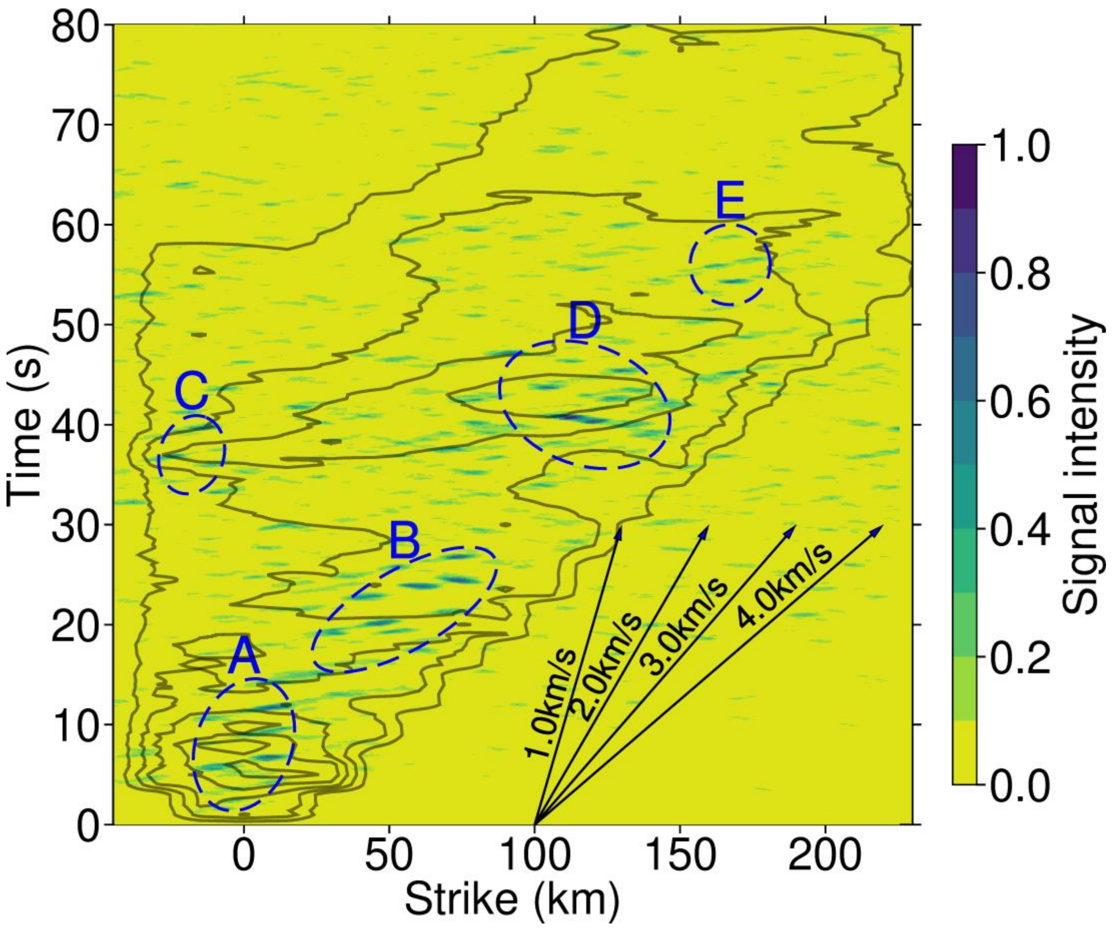

Figure 5: Spatiotemporal evolution of normalized high-frequency radiation along the strike direction in the primary N1 fault plane. The color represents the normalized strength of high-frequency radiation. The blue dashed lines denote high-frequency events. The black contour interval of the slip-rate is 0.03m/s. The black arrows show the reference rupture speeds.

From 15 to 45 s, a high-slip-rate area appears to the north of the epicenter (15 to 30 s) that then expands bilaterally, both northward and southward, from 30 to 45 s (Fig. 5). During this rupture stage, we observe the strong BP signals of event B during 15 to 30 s at ~60 km north of the epicenter, just before the rupture begins to propagate bilaterally both northward and southward from the epicenter. To evaluate event B in more detail, we examined snapshots obtained in 2-s steps from 20 s to 40 s (Fig. S3). The BP signals marked as event B in the high-slip-rate area become stronger from 20 to 28 s, but subsequently the event B signals decrease rapidly and disappear at 30 s. After event B, the high-slip-rate area migrates bilaterally, but dominantly southward, from the event B area (Figs. S3 and 5). Thus, event B is interpreted as bilateral rupture acceleration, including back-rupture propagation toward the south. During the southward back-rupture propagation, the strong BP signals of event C are observed at 35 s, around 25 km south of the epicenter (Fig. 5). Because event C is at the southern edge of the rupture zone, where the slip rate decreases, it must correspond to the deceleration or termination of the southward back-propagating rupture. Notably, the IRIS-DMC automated BP product also shows weak BP signals corresponding to event C at 30 to 40 s near the epicenter (http://ds.iris.edu/spud/backprojection/17616500). Furthermore, Vallée et al. (2020), using the Multitaper-MUSIC BP method (Meng et al., 2011) independently found similar high-frequency signal emissions back-propagating from north to south of the epicenter. If the BP signals of events B and C are the signature of continuous back-propagation from north to south of the epicenter, then the rupture-front velocity can be estimated as approximately at 4 km/s (0.85 V_S) (V_S is the shear wave velocity) along the strike of the fault plane (Fig. 5). Our observation of the back-rupture propagation is similar to what is proposed in the numerical simulations (Gabriel et al., 2012; Idini & Ampuero, 2020) and the recent finding during the M_W 7.1 2016 Romanche transform earthquake (Hicks et al., 2020). Alternatively, a rupture path with a slow rupture-front velocity of 1 km/s could be drawn directly from events A to C, instead of from B to C, (Fig. 5). Although it is difficult to completely exclude this possibility, the fact that we do not observe clearer or stronger BP signals along the possible rupture path from A to C than along the path from B to C, supports the likelihood of a southward back-propagating rupture. It is also possible that in a narrow model space, such an apparent, sudden stop of the southern rupture behavior might be artificially observed by finite-fault inversion. We tested this hypothesis by adopting a longer model space, adding 60 km to the model plane length south of the epicenter, and we confirmed that, consistent with the rupture behavior in the shorter model space, the southward rupture robustly stopped at ~30 km south of the epicenter (Fig. S7).

Following the north-south bilateral rupture, the rupture pattern returns to northern unilateral propagation. At 40 s, we observe the strong BP signals of event D at ~110 km north of the epicenter (Fig. 5). The high-slip rate associated with event D at 100 km north of the epicenter can therefore correspond to rapid northward rupture acceleration. After the moderate BP signal of event E is observed in the updip part of the fault plane, the rupture propagation finally halts in the area ~200 km north of the epicenter. Thus, event E can correspond to rupture deceleration at the northern edge of the fault plane, indicating termination of the rupture.

The distribution of T-axis azimuths, extracted from the resultant potency-density tensors, shows gradual clockwise rotation from the epicenter northward, and the large-slip area from 50 to 150 km north of the hypocenter corresponds to the high curvature area of the slab iso-depth lines (Fig. 6). The synthetic test showed that the T-axis azimuth rotation was well restored in the output model (Fig. S4b). The rotation of the T-axis azimuths is well correlated with that of the slab strike. In general, accumulation of extensional stress associated with slab bending is one cause of intraslab earthquakes (e.g., Astiz et al., 1988; Okuwaki and Yagi, 2017). The apparent consistency between the T-axis azimuths and the slab geometry suggests that the 2019 Peru earthquake was caused by extensional stress generated by the slab bending and that the rupture process of the 2019 Peru earthquake was controlled by the slab geometry. While, Ranero et al. (2005) found that, in Middle America and Chile subduction zones, the patterns of nodal-planes orientation of intermediate-depth earthquakes in slab is similar to those of the near-trench bending-related earthquakes, which is not consistent with the slab geometry, suggesting that the intermediate-seismicity is a result of reactivation of faults formed by the plate bending near the trench. Given the possible uncertainty of slab-geometry model and the limited seismicity in the source region of the 2019 Peru earthquake, however, it is difficult to uniquely eliminate either the possibility of fault reactivation or the slab bending for the occurrence of the 2019 Peru earthquake alone, and a future study, together with a high-resolution bathymetry map of the sea-floor fabric, will evaluate whether this rotation of the T-axis azimuth along ~200-km-long fault is a result of fault reactivation.

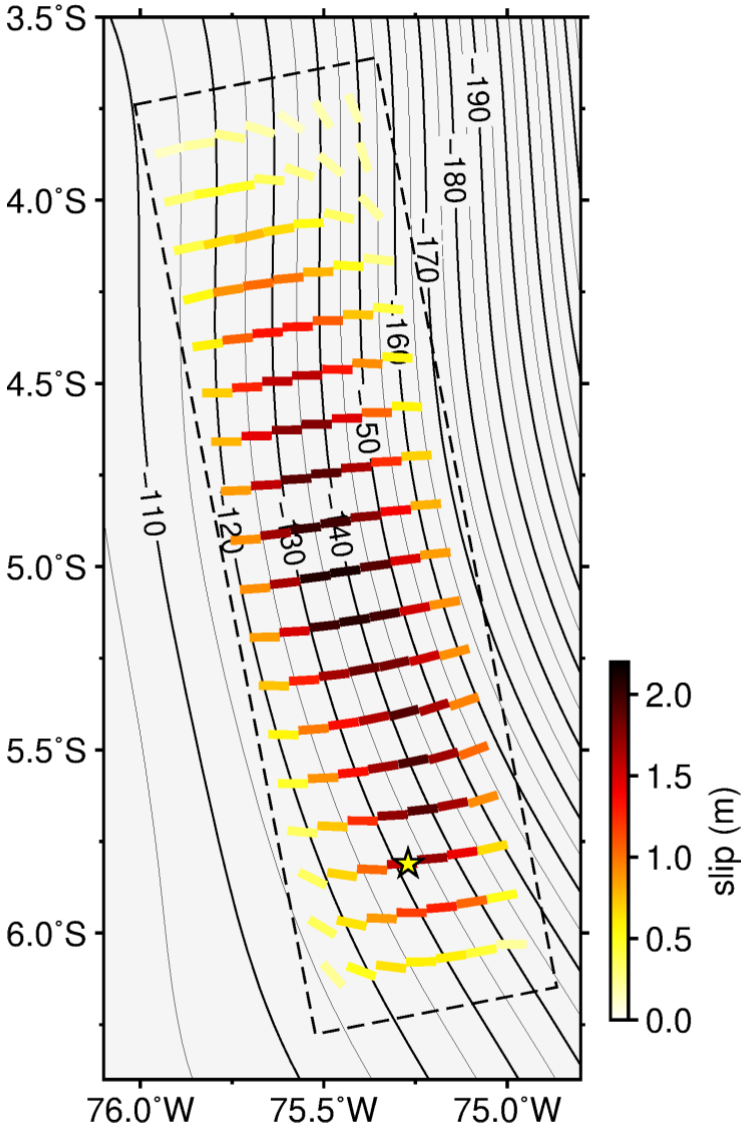

Figure 6: Spatial distribution of T-axis azimuth distribution. The black dashed rectangle indicates the primary fault plane. The black contours are iso-depths (km) of Slab2 model (Hayes et al., 2018). The yellow star shows the epicenter. The dashed rectangle outlines the fault plane.

The inverted source model shows a complex rupture pattern, including back-rupture propagation and the rotation of T-axis azimuth, but the total slip distribution in the inverted model was smoother than in previous studies (e.g., Liu and Yao, 2020; Ye et al., 2020). This difference in smoothing may be explained by the fact that we used a seismic source model with high degrees of freedom and determined the optimal values of the hyperparameters, including smoothing strength, by minimizing Akaike's Bayesian Information Criterion (Akaike, 1980; Yabuki and Matsu'ura, 1992; Yagi and Fukahata, 2011). It is worth noting that the smooth source model is well able to explain the characteristics of the observed velocity waveforms, including the high-frequency component (Fig. S2).

5. Conclusion

We applied a newly developed finite-fault teleseismic waveform inversion method and the BP method to estimate the detailed rupture process of the 2019 Peru intraslab earthquake. Integrated use of the finite-fault inversion and BP methods made it feasible to select the primary fault plane of the main shock, because the finite-fault inversion and the BP were consistent in showing eastward rupture propagation only on an east-dipping fault plane during the rupture process. Our study revealed that the 2019 Peru earthquake ruptured a steeply dipping normal fault with multiple rupture episodes. The initial downdip and eastward rupture episode around the hypocenter was followed by a northward rupture episode. Then, the main bilateral rupture episode propagated both northward and southward of the epicenter and was followed by a unilateral northward rupture episode. Most notably, the southern wing of the main bilateral rupture back-propagated through the initial rupture area. The estimated potency-density tensor for each source element in the finite-fault model revealed that the clockwise rotation of T-axis azimuths corresponded well to the change in the strike of the Nazca slab in the large-slip area. These findings suggest that the 2019 Peru earthquake resulted from extensional stress generated by slab bending.

Acknowledgements

We thank the editor and the reviewers for evaluating the manuscript. This work was supported by a Grant-in-Aid for Scientific Research (C) 19K04030. The facilities of IRIS Data Services, and specifically the IRIS Data Management Center, were used for access to waveforms, related metadata, and derived products used in this study. IRIS Data Services are funded through the Seismological Facilities for the Advancement of Geoscience (SAGE) Award of the National Science Foundation under Cooperative Support Agreement EAR-1851048. All of the figures were generated with Generic Mapping Tools (Wessel et al., 2013). Waveform data were downloaded via the IRIS Wilber 3 system (https://ds.iris.edu/wilber3). Teleseismic waveforms were obtained from the following networks: the Canadian National Seismograph Network (CN; https://doi.org/10.7914/SN/CN); the GEOFON Seismic Network (GE; https://doi.org/10.14470/TR560404); the Netherlands Seismic and Acoustic Network (NL; https://doi.org/10.21944/e970fd34-23b9-3411-b366-e4f72877d2c5); the GEOSCOPE (G; https://doi.org/10.18715/GEOSCOPE.G); the IRIS/IDA Seismic Network (II; https://doi.org/10.7914/SN/II); the International Miscellaneous Stations (IM; https://www.fdsn.org/networks/detail/IM/); the Global Seismograph Network (IU; https://doi.org/10.7914/SN/IU), the Global Telemetered Seismograph Network (GT; https://doi.org/10.7914/SN/GT) and the Berkeley Digital Seismograph Network (BK; https://doi.org/10.7932/BDSN).

References

Akaike, H., 1980. Likelihood and the Bayes procedure, Trabajos de Estadistica y de Investigacion Operativa 31(1), 143–166, doi: 10.1007/BF02888350.

Astiz, L., Lay, T., Kanamori, H., 1988. Large intermediate-depth earthquakes and the subduction process, Phys. Earth Planet. Inter., 53(1-2), 80-166, doi: 10.1016/0031-9201(88)90138-0.

Chang, Y., Warren, L. M., Zhu, L., Prieto, G. A., 2019. Earthquake Focal Mechanisms and Stress Field for the Intermediate-Depth Cauca Cluster, Colombia, J. Geophys. Res. Solid Earth, 124, 822-836, doi: 10.1029/2018JB016804.

DeMats, C., Gordon, R. G., & Argus, D. F., 2010. Geologically current plate motions, Geophys. J. Int., 181(1) 1-80, doi: 10.1111/j.1365-246X.2009.04491.x.

Duputel, Z., Agram, P.S., Simons, M., Minson, S.E. & Beck, J.L., 2014. Accounting for prediction uncertainty when inferring subsurface fault slip, Geophys. J. Int., 197(1), 464–482, doi: 10.1093/gji/ggt517.

Dziewonski, A.M., Chou, T.A., Woodhouse, J.H., 1981. Determination of earthquake source parameters from waveform data for studies of global and regional seismicity, J. Geophys. Res., 86, 2825-2852, doi: 10.1029/JB086iB04p02825.

Ekström, G., Nettles, M., Dziewoński, A.M., 2012. The global GMT project 2004-2010: Centroid-moment tensors for 13,017 earthquakes, Earth Planet. Sci. Lett., 200-201, 1-9, doi: 10.1016/j.pepi.2012.04.002.

Gabriel, A. A., Ampuero, J., P., Dalguer, L. A., Mai, P. M., 2012. The transition of dynamic rupture styles in elastic media under velocity-weakening friction, J. Geophys. Res., 117, B09311, doi: 10.1029/2012JB009468.

Hartzell, S. H. and Heaton, T. H., 1983. Inversion of strong ground motion and teleseismic waveform data for the fault rupture history of the 1979 Imperial Valley, California, earthquake, Bull. Seismol. Soc. Am., 73(6), 1553–1583.

Hayes, G. P., Moore, G. L., Portner, D. E., Hearne, M., Flamme, H., Furtney, M., Smoczyk, G. M., 2018. Slab2 - A Comprehensive Subduction Zone Geometry Model, Science, 362, 58-61, doi: 10.1126/science.aat4723.

Hicks, S.P., Okuwaki, R., Steinberg, A. et al., 2020. Back-propagating supershear rupture in the 2016 Mw 7.1 Romanche transform fault earthquake, Nat. Geosci., 13, 647–653, do: 10.1038/s41561-020-0619-9.

Idini, B., & Ampuero, J. P., 2020. Fault-zone damage promotes pulse-like rupture and rapid-tremor-reversals, Geophys. Res. Lett., 47, e2020GL090736, doi: 10.31223/osf.io/v8xr2.

Ishii M., Shearer P.M., Houston H., Vidale J.E., 2005. Extent, duration and speed of the 2004 Sumatra–Andaman earthquake imaged by the Hi-Net array, Nature, 435(7044), 933–936, doi: 10.1038/nature03675.

Julian, B. R., Miller A. D., and Foulger G. R., 1998. Non-double couple earthquakes: 1. Theory. Rev. Geophys., 36, 525– 549, doi: 10.1029/98RG00716.

Kaila, K. L., Krishna, V. G., Khandekar, G., 1999. Preliminary models of upper mantle P and S wave velocity structure in the western South America region, J. Geodynamics, 27, 567-583, doi: 10.1016/S0264-3707(98)00016-7.

Kennett, B. L. N., Engdahl, E. R., Buland, R., 1995. Constraints on seismic velocities in the Earth from traveltimes, Geophys. J. Int., 122(1), 108-124, doi: 10.1111/j.1365-246X.1995.tb03540.x.

Kikuchi, M. & Kanamori, H., 1991. Inversion of Complex Body Waves-III, Bull. Seismol. Soc. Am., 81(6), 2335–2350.

Kiser, E., and Ishii, M., 2017. Back-projection Imaging of Earthquakes, Annu. Rev. Earth Planet. Sci., 45, 271-299, doi: 10.1146/annurev-earth-063016-015801.

Krüger, F. & Ohrnberger, M., 2005. Spatio-temporal source characteristics of the 26 December 2004 Sumatra earthquake as imaged by teleseismic broadband arrays, Geophys. Res. Lett., 32(24), L24312, doi: 10.1029/2005GL023939.

Legrand, D., and Delouis, B., 1999. Determination of the fault plane using a single near-field seismic station with a finite dimension source model, Geophys. J. Int., 138, 801-808, doi: 10.1046/j.1365-246x.1999.00917.x.

Liu, W., and Yao, H., 2020. Rupture process of the 26 May 2019 Mw 8.0 northern Peru intermediate-depth earthquake and insights into its mechanism, Geophys. Res. Lett., 47, e2020GL087167, doi: 10.1029/2020GL087167.

Ma, Y., Clayton, R. W., 2014. The crust and uppermost mantle structure of Southern Peru from ambient noise and earthquake surface wave analysis, Earth Planet. Sci. Lett., 395, 61-70, doi: 10.1016/j.epsl.2014.03.013.

Madariaga, R., 1977. High-frequency radiation from crack (stress drop) models of earthquake faulting, Geophys. J. Int., 51(3), 625-651, doi: 10.1111/j.1365-246X.1977.tb04211.x.

Meng, L., Inbal, A., and Ampuero, J.-P., 2011. A window into the complexity of the dynamic rupture of the 2011 Mw 9 Tohoku-Oki earthquake, Geophys. Res. Lett., 38, L00G07, doi: 10.1029/2011GL048118.

Muirhead, K. T., Datt, R., 1976. The N-th root process applied to seismic array data, Geophys. J. Int., 47, 197– 210, doi: 10.1111/j.1365-246X.1976.tb01269.x.

Okuwaki, R. and Yagi, Y., 2017. Rupture process during the Mw 8.1 2017 Chiapas Mexico earthquake: Shallow intraplate normal faulting by slab bending, Geophys. Res. Lett., 44, 11,816–11,823, doi: 10.1002/2017GL075956.

Okuwaki, R., Yagi Y., Hirano S., 2014. Relationship between high-frequency radiation and asperity ruptures, revealed by hybrid back-projection with a non-planar fault model, Sci. Rep., 4(1), 1–6, doi: 10.1038/srep07120.

Olson, A. H. and Apsel, R. J., 1982. Finite faults and inverse theory with applications to the 1979 Imperial Valley earthquake, Bull. Seismol. Soc. Am., 72(6), 1969–2001.

Perfettini, H., Avouac, JP., Tavera, H., Kositsky, A., Nocquet JM., Bondoux, F., Chlieh, M., Sladen, A., Audin, L., Farber, D. L., Soler, P., 2010. Seismic and aseismic slip on the Central Peru megathrust, Nature, 465, 78–81, doi: 10.1038/nature09062.

Prezzi, C., Silbergleit, V., 2015. Seismic hazards along Ecuador, Peru and northern Chile (South America), Nat. Hazards, 79(2), 1159-1175, doi: 10.1007/s11069-015-1900-x.

Ragon, T., Sladen, A., and Simons, M., 2018. Accounting for uncertain fault geometry in earthquake source inversions – I: theory and simplified application, Geophys. J. Int., 214 (2), 1174–1190, doi: 10.1093/gji/ggy187.

Ranero, C.R., Villaseñor, A., Phipps Morgan, J., Weinrebe, W., 2005. Relationship between bend-faulting at trenches and intermediate-depth seismicity, Geochem. Geophys. Geosyst., 6 (12), doi: 10.1029/2005GC000997.

Shimizu, K., Yagi, Y., Okuwaki, R. Fukahata, Y., 2020. Development of an inversion method to extract information on fault geometry from teleseismic data, Geophys. J. Int., 220 (2), 1055-1065, doi: 10.1093/gji/ggz496.

Sladen, A., Tavera, H., Simons, M., Avouac, J. P., Konca, A. O., Perfettini, H., Audin, L., Fielding, E. J., Ortega, F., and Cavagnoud, R., 2010. Source model of the 2007 Mw 8.0 Pisco, Peru earthquake: Implications for seismogenic behavior of subduction megathrusts, J. Geophys. Res., 115, B02405, doi: 10.1029/2009JB006429.

Somoza, R., Ghidella, M., 2005. Convergencia en el margen occidental de América del Sur durante el Cenozoico: subducción de las placas de Nazca, Farallón y Aluk. Rev. Asoci. Geol. Argentina, 60, 797–809.

Spudich, P. and Frazer, L. N., 1984. Use of ray theory to calculate high-frequency radiation from earthquake sources having spatially variable rupture velocity and stress drop, Bull. Seismol. Soc. Am., 74(6), 2061-2082.

Suzuki, M., and Yagi, Y., 2011. Depth dependence of rupture velocity in deep earthquakes, Geophys. Res. Lett., 38, L05308, doi: 10.1029/2011GL046807.

Tavera, H. & Buforn, E., 2001. Source mechanism of earthquakes in Peru, J. Seismol., 5, 519-539, doi: 10.1023/A:1012027430555.

Uchide, T., Yao H., Shearer P.M., 2013. Spatio-temporal distribution of fault slip and high-frequency radiation of the 2010 El Mayor-Cucapah, Mexico earthquake, J. geophys. Res. Solid Earth, 118(4), 1546–1555, doi: 10.1002/jgrb.50144.

Vallée, M., Grandin, R., Nocquet, J.-M., Villegas, J.-C., Vaca, S., Xie, Y., Meng, L., Ampuero, J.-P., Mothes, P., and Jarrin, P., 2020. Rupture characteristics of the 2019 North Peru intraslab earthquake (Mw8.0), EGU General Assembly 2020, Online, 4–8 May 2020, EGU2020-10429, doi: 10.5194/egusphere-egu2020-10429.

Villegas-Lanza, J. Chlieh, M., Cavalié, O., Tavera, H., Baby, P., Chire-Chira, J. and Nocquet, J., 2016. Active tectonics of Peru: Heterogeneous interseismic coupling along the Nazca megathrust, rigid motion of the Peruvian Sliver, and Subandean shortening accommodation, J. Geophys. Res., Solid Earth 121, 7371–7394, doi: 10.1002/2016JB013080.

Wang, K., Wada, I., Ishikawa, Y., 2004. Stresses in the subducting slab beneath southwest Japan and relation with plate geometry, tectonic forces, slab dehydration, and damaging earthquakes, J. Geophys. Res. Solid Earth, 109, B8, doi: 10.1029/2003JB002888.

Wessel, P., Smith, W.H.F., Scharroo, R., Luis, J., Wobbe, F., 2013. Generic Mapping Tools: improved version released. Eos. Trans, AGU 94-45 (2013), pp., 409-410, doi: 10.1002/2013EO450001.

Wong, I., Dober, M., Hemphill-Haley, M., Terra, F., 2012. Seismic hazard along the southern coast of Ecuador. In: Proceedings of the fifthteenth world conference on earthquake engineering, Lisbon p 10.

Yabuki, T. & Matsu'ura, M., 1992. Geodetic data inversion using a Bayesian information criterion for spatial distribution of fault slip. Geophys, J. Int., 109(2), 363–375, doi: 10.1111/j.1365-246X.1992.tb00102.x.

Yagi, Y. & Fukahata, Y., 2011. Introduction of uncertainty of Green's function into waveform inversion for seismic source processes. Geophys, J. Int., 186(2), 711–720, doi: 10.1111/j.1365-246X.2011.05043.x.

Yagi, Y. and Okuwaki, R., 2015. Integrated seismic source model of the 2015 Gorkha, Nepal, earthquake, Geophys. Res. Lett., 42(15), 6229-6235, doi: 10.1002/2015GL064995.

Yagi, Y., Mikumo T., Pacheco J., and Reyes G., 2004. Source rupture process of the Tecoman, Colima, Mexico Earthquake of 22 January 2003, determined by joint inversion of teleseismic body-wave and near-source data. Bull, Seismol. Soc. Am., 94, 1795–1807, doi: 10.1785/012003095.

Yagi, Y., Nakao, A., & Kasahara, A., 2012. Smooth and rapid slip near the Japan Trench during the 2011 Tohoku-oki earthquake revealed by a hybrid back-projection method, Earth planet. Sci. Lett., 355-356, 94–101, doi: 10.1016/j.epsl.2012.08.018.

Ye, L., Lay, T., Kanamori, H., 2020. Anomalously low aftershock productivity of the 2019 Mw 8.0 energetic intermediate-depth faulting beneath Peru, Earth planet. Sci. Lett., 549, 116528, doi: 10.1016/j.epsl.2020.116528.